High-Performance Supported Ir-Oxohydroxide Water Oxidation Electrocatalysts

C. Massué,[a,b] V. Pfeifer,[a] X. Huang,[a] J. Noack,[a] A. Tarasov,[a] S. Cap*[a] and R. Schlögl[a,b]

Abstract: The synthesis of a highly active and yet stable electrocatalyst for the anodic oxygen evolution reaction (OER) remains a major challenge for acidic water splitting on an industrial scale. Addressing this challenge, we obtained an outstanding high-performance OER-catalyst by loading Ir on conductive antimony-doped tin oxide (ATO)-nanoparticles via a microwave (MW)-supported hydrothermal route. The obtained Ir-phase was identified as an XRD-amorphous, highly hydrated $Ir^{III/IV}$-oxohydroxide. In order to identify chemical and structural features responsible for the high activity and exceptional stability under acidic OER-conditions at loadings as low as 20 μg_{Ir} cm^{-2}, we used stepwise thermal treatment to gradually alter the XRD-amorphous Ir-phase via dehydroxylation and crystallization of IrO_2. This resulted in dramatic depletion of OER-performance, indicating that the outstanding electrocatalytic properties of the MW-produced $Ir^{III/IV}$-oxohydroxide are prominently linked to the nature of the produced Ir-phase. This finding is in contrast with the often reported stable but poor OER-performance of crystalline IrO_2-based compounds produced via more classical calcination routes. Our investigation demonstrates the immense potential of Ir-oxohydroxide-based OER electrocatalysts for stable high-current water electrolysis under acidic conditions.

1. Introduction

Chemical energy storage through hydrogen production from water splitting has come under focus as one of the most promising answers to the transient nature of renewable energy sources.[1, 2] The electrocatalytic splitting of water can be driven by any type of power supply and its combination with intermittent renewable sources could ensure the storage of excess energy in the chemical bond of hydrogen. Electrolyzer setups are being seen as a particularly versatile solution as they could be implemented into smart grids running on a variety of power sources on a de-centralized level.[1] In particular, proton exchange membrane (PEM)-based electrolyzers allow for the production of high-purity H_2 at elevated pressure in compact designs.[3] The efficient separation of O_2 and H_2 produced respectively in the anodic and cathodic compartments is ensured by polymeric membranes featuring proton exchange capabilities, *e.g.,* Nafion®. However, these sulfonic-acid-functionalized membranes require a highly acidic environment. The resulting corrosive conditions pose a major challenge to the employed electrocatalysts, especially for the anodic oxygen evolution reaction (OER).

The optimization of an active and stable and yet cost-effective OER-electrocatalyst material has emerged as one of the toughest hurdles in the design of a commercially relevant PEM-electrolyzer system. Earth-abundant transition metal oxides such as Co_3O_4, Fe_2O_3 and MnO_x show low activity and minimal stability under acidic OER-conditions[3] and even more active Ru-based anodes have been shown to corrode at fast rates.[4, 5] The only promising candidates so far are Ir-based compounds, which seem to be able to combine high activity with relative stability under acidic OER-conditions.[5] Due to the scarcity of iridium and resulting high material costs, the minimization of the anodic Ir-loading is of outmost importance in making Ir-based anodes a financially viable solution. In this regard, a classical strategy is to maximize the electrocatalytically active surface area by means of dispersing iridium on a conductive support.

Ir-dispersion for electrocatalytic performance enhancement should be performed on a conductive support which remains stable under acidic OER-conditions. Reier et al. have recently highlighted the potential of inexpensive carbon black used to support Ir-nanoparticles as they observed a sevenfold increase in the number of OER-active sites over bulk Ir.[6] However, low stability under OER-conditions was also reported along with fast corrosion of the carbon-support. Yi et al. recently showed that fast oxidative degradation is common to all carbon materials at anodic potentials in acidic electrolytes, banning such supports from use in acidic OER.[7] More stable alternatives to carbonaceous supports include conductive doped tin oxides. In particular antimony-doped tin oxide (ATO) is known for its stability under anodic potentials in chlorine-free acidic electrolytes.[8] In ATO, quasi-metallic n-type conductivity is achieved by doping SnO_2 with approx. 5% Sb.[9, 10] ATO has the advantage of being cheaper than indium-doped tin oxide (ITO) and can be synthesized via wet chemical routes involving safe precursors, unlike fluorine-doped tin oxide (FTO).[11] A method of choice for ATO-synthesis is hydrothermal synthesis due to small resulting particle sizes.[10, 12] ATO has been successfully employed as a support for precious metal OER-catalyst under acidic conditions. For instance, Tseung and Dhara studied Pt supported on ATO versus carbon black under harsh conditions in H_3PO_4 at 150°C.[13] They showed that the highest stability under potentiostatic conditions was achieved for ATO-supported Pt electrocatalysts. Similarly, Liu et al. reported significant OER-activity enhancement of ATO-supported IrO_2-nanoparticles over bulk IrO_2 due to higher Ir-dispersion and a resulting higher electrochemically active surface area.[14]

In addition to optimized catalyst morphology via dispersion of Ir-particles on a suitable support, producing the “right” chemical state of iridium is no less critical to the OER-performance of the

[a] C. Massué, V. Pfeifer, Dr. X. Huang, Dr. J. Noack, Dr. A. Tarasov, Dr. S. Cap, Prof. Dr. R. Schlögl
Department of Inorganic Chemistry
Fritz Haber Institute of the Max Planck Society
Faradayweg 4-6, 14195 Berlin (Germany)
E-mail: sebastiencap@fhi-berlin.mpg.de
[b] Prof. Dr. R. Schlögl
Department of Heterogenous Reactions
Max Planck Institute for Chemical Energy Conversion
Stiftstrasse 34-36, 45470 Mülheim-an-der-Ruhr (Germany)

Supporting information for this article is given via a link at the end of the document

catalytic system. Early electrochemical studies have shown that metallic iridium is inefficient in OER and needs to be activated under oxidative conditions.[2, 15-19] Synthesis strategies often include calcination steps above 400°C, which leads to crystalline IrO_2.[20-27] Such crystalline IrO_2-compounds exhibit high stability, which has established them as a target material for OER-catalysis.[28] Unfortunately, the limited Ir-mass specific OER-activity of IrO_2 results in high anodic loadings in the order of 2 mg_{Ir} cm^{-2}.[29]

An in-depth literature survey suggests a more cost-effective alternative in the form of amorphous, oxide/hydroxide Ir-phases combining superior intrinsic activity with stability under acidic OER-conditions.[30-35] *E.g.*, Reier et al. showed that Ir-acetate calcined at 250°C yielded amorphous Ir-oxide/hydroxide species combining both activity and relative stability in acidic OER.[36] Higher thermal treatment had a detrimental effect on OER-performance, as crystalline IrO_2 was forming. The formation of crystalline IrO_2 upon thermal treatment under dry conditions is a general problem when aiming for amorphous Ir-phases. In addition such phases have proven elusive to characterization. Amorphous Ir-oxide/hydroxides are easily reduced under standard TEM-electron beam conditions [37], rendering direct observation difficult. Additionally, chemical information on Ir-species is difficult to extract from X-ray photoelectron spectroscopy as the debate on lineshape and binding energies of various Ir-species is still ongoing[38-40]. Such issues in preparing and characterzing amorphous Ir-oxide/hydroxides might explain the lack of attention they have received so far.

The present study has taken advantage of microwave-assisted (MW) hydrothermal synthesis methodology, which constitutes a method of choice when aiming for the preparation of nanostructured and highly hydroxylated oxide phases.[41] As synthetic target, we chose to load a conductive ATO-support with 30 mol.% amorphous Ir-oxide/hydroxide. For this purpose, a basic suspension of ATO-nanoparticles, containing dissolved Ir-precursors was treated in a MW-assisted hydrothermal synthesis reactor. The nature of the resulting amorphous Ir-nanoparticles on ATO was analyzed via a combination of various physico-chemical characterization methods, including the analysis of XPS-data based on a recent model allowing for an accurate speciation of Ir.[36, 42, 43] The OER-performance of the synthetized compound was compared to commercially available benchmarks and literature references. In an effort to uncover the relevance of the Ir-phase for OER-performance, we thermally altered the MW-produced Ir-based catalyst via dehydroxylation and crystallization under O_2 and Ar atmosphere at 250 and 350 °C. Such extended methodology of previous work[44, 45] allows uncovering the OER-relevant features of the MW-synthesized Ir-oxide/hydroxide compound by relating the evolution of OER-performance to structural and chemical changes obtained via thermal alteration. The results should answer the question whether Ir-oxide/hydroxides can substitute crystalline IrO_2 as more efficient electrocatalysts for acidic OER.

Table 1. Sample designations used throughout the text and brief description.

Samples label	Description
MW-ATO	Selected ATO-support prepared via MW-supported hydrothermal synthesis at 270°C
MW-Ir/ATO	30mol.% Ir loaded on MW-ATO via MW-supported synthesis at 250°C
Ir_250C_O_2	MW-Ir/ATO, calcined 250°C, 21%O_2/Ar
Ir_250C_Ar	MW-Ir/ATO, calcined 250°C, Ar
Ir_350C_O_2	MW-Ir/ATO, calcined 350°C, 21%O_2/Ar
Ir_350C_Ar	MW-Ir/ATO, calcined 350°C, Ar
SA-IrO_2	Crystalline IrO_2-benchmark
AA-IrO_x	Amorphous IrO_x-benchmark

2. Results and Discussion

2.1 Catalyst support (ATO) synthesis and characterization

In order to synthesize a high surface-area ATO-compound, we adapted the hydrothermal synthesis of Nütz et al.[10, 12] In summary, the first synthesis-step involves the peptization of a Sb^{III}/Sn^{IV}-chloride solution adjusted to a pH value of 4 using 1%-NH_3/H_2O. We selected a 5%-Sb-doping level based on literature reports indicating that above 7-9%, Sb tends to segregate from the ATO-phase.[12, 46, 47] The hydrolyzed Sn/Sb-suspension was treated at various temperatures between 180 and 290°C for 1h. Note that Nütz et al. used a classical autoclave, which required higher treatment times of up to 16h.[10, 12] The resulting dried products were analyzed via XRD and show a pattern associated with the rutile structure of SnO_2 cassiterite (Figure S1). No pattern associated with a segregated Sb-oxide phase could be detected, which indicates successful implementation of Sb into the cassiterite lattice. The Sb-doping of the ATO samples, synthetized within a temperature range of 180 to 270°C was assessed via diffuse reflectance (DR) UV-Vis spectroscopy (Figure 1). In addition, for qualitative comparison two commercial reference samples, one crystalline SnO_2 (Aldrich, 99.9%) and one conductive ATO (Aldrich, 99.5%) are also reported.

All samples show adsorption in the UV-range below 320 nm, which corresponds to the valence-to-conduction band transition.[10] As expected, the undoped SnO_2–benchmark shows no absorption in the infrared (IR) region, whereas the ATO-benchmark features a broad absorption above 1500 nm corresponding to successful n-type Sb^V-doping. [9] The MW-produced ATO shows a growing IR-absorption features with increasing the synthesis temperature and reaches a maximum, i.e., highest level of Sb^V-doping, at temperatures between 270 and 290°C. Comparison of absolute spectral intensities between MW-produced samples and the benchmarks is pointless as different sample morphologies play an important role in the scattering process and modify the intensities.

Supporting the DR-UV-Vis results, the sample conductivities were measured via the classical four-point-probe contact

measurement technique on pressed powder pellets. The highest conductivities for the MW-produced samples correlate well with the highest absorption band in the IR. Resistivities of 17 and 11 Ω.cm were measured for the ATO prepared at 270 and 290°C, respectively (see Table S1). These results compare well to values reported in the literature [12, 48] and to the ATO-benchmark (20 Ω cm). The energy-dispersive X-ray spectroscopy of the MW-ATO, recorded on random agglomerates in Scanning Electron Microscopy (SEM-EDX) confirmed a homogenous Sb-distribution inside the SnO_2-matrix at 5.0% (see Figure S2). TEM-images show a homogenous material consisting of small, approx. 5 nm-particles (see Figure S3), which is well in-line with the broad XRD-peaks and the high specific surface area measured. For further use, the ATO prepared at 270°C was chosen as the conductive OER-catalyst support MW-ATO, as it exhibited the highest specific surface area (S_{BET}) with 207 m^2 g^{-1} (Table S1).

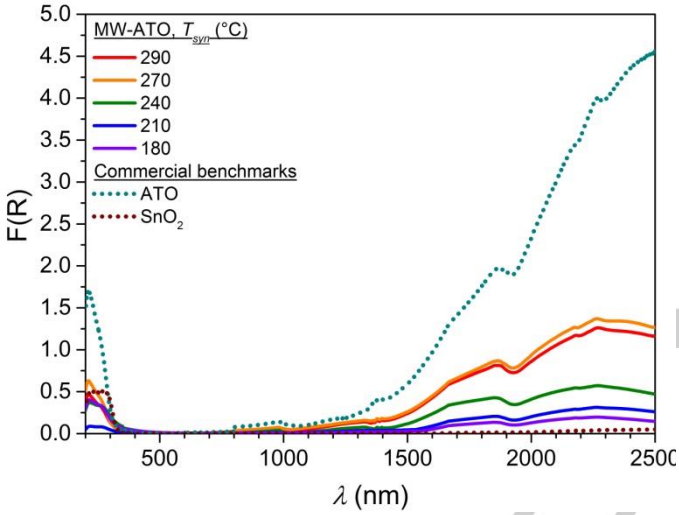

Figure 1. Diffuse reflectance UV-Vis spectra of SnO_2- and ATO-benchmarks (dotted lines) and ATO obtained via the MW-treatment of a colloidal Sb/Sn-suspension at various temperatures (full lines).

2.2 MW-assisted hydrothermal synthesis of MW-Ir/ATO

A 30 mol.% Ir-loading was selected as an optimum target based on the work of Pauli et al.[20, 21] and Balko et al.[49] The loading of the MW-ATO support was achieved using K_2IrCl_6 dissolved in an aqueous suspension of MW-ATO raised to pH=13 with a concentrated KOH-solution. At such basic pH, Ir-cations are readily adsorbed on ATO due the low isoelectric point of Sn-based compounds.[50] The Ir-hydrolysis was performed under MW-supported hydrothermal synthesis conditions at 250°C for 1h. The resulting solid product was centrifuged, repeatedly washed and dried.

The hydrolysis step is crucial as chloroiridate(IV)-complexes are stable in acidic or neutral solutions up to high temperatures and do not yield a solid product after hydrothermal treatment.[51] In presence of base, $IrCl_6^{2-}$, which is a well-known outer-sphere oxidant, first reduces to $IrCl_6^{3-}$ via water oxidation[52] . This phenomenon is evidenced by the formation of O_2-bubbles and by the discoloration of the solution from red-brown to pale yellowish, due to the loss of the $IrCl_6^{2-}$ ligand-to-metal-charge-transfer-bands (LMCT).[53] The subsequent hydrolysis of $IrCl_6^{3-}$ is a slow process occurring over days at room temperature and is still incompletely understood with respect to the suspected formation of mixed-valence iridium oligomers.[51, 53, 54] The MW-treatment greatly accelerates this process, while avoiding thermal treatment under dry conditions, which would easily lead to the formation of crystalline IrO_2.

2.2.1. OER-performance of MW-Ir/ATO

In order to assess the OER-performance of the obtained MW-Ir/ATO, the powder was loaded onto a rotating disk electrode (RDE) implemented into a standard three-compartment cell containing a 1 mol L^{-1} H_2SO_4 electrolyte. The OER-performance of MW-Ir/ATO was assessed via a chronopotentiommetric (CP)-test at 10mA cm^{-2} (Figure 2). This procedure has been used in recent benchmarking efforts in order to reference the most promising OER-catalysts[5, 55]. We also tested a commercially available amorphous Ir-oxide/hydroxide benchmark (AA-IrO_x) used by Pfeifer et al. in their study of the electronic structure of Ir-oxides[42, 43] and which is speculated to be close in nature to MW-Ir/ATO. In addition, a powdered IrO_2-benchmark (SA-IrO_2) was used a crystalline benchmark.

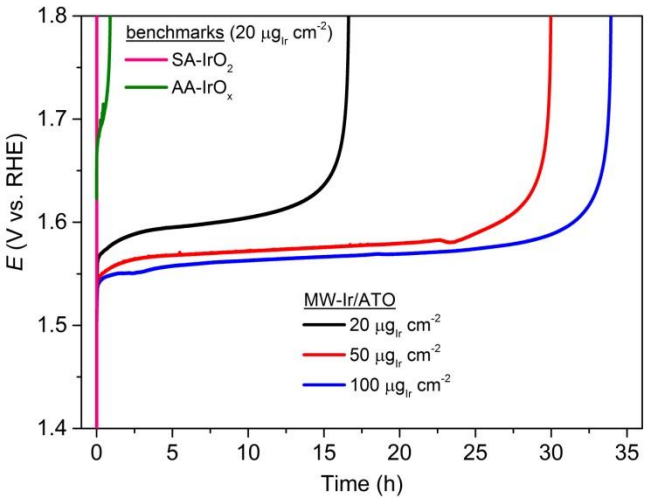

Figure 2. CP-based OER-performance tests at j = 10 mA cm^{-2} for MW-Ir/ATO with three loadings, 20, 50 and 100 μg_{Ir} cm^{-2}, and for the two commercial benchmarks, AA-IrO_x and SA-IrO_2.

The overpotentials η needed to maintain a current density of j = 10 mA cm^{-2} after various periods of time were extracted from the potential vs. time curves shown in Figure 2 and reported as OER-performance indicators in Table 2. A stable overpotential means that the catalytic activity of the electrocatalyst remains stable over time. Deactivation of the catalytic activity usually occurs in two steps (Figure 2): First, depletion of the intrinsic catalytic activity that translates into a slow gradual increase of anodic potentials required to maintain the current density at the set value (10 mA cm^{-2}). Once anodic potentials of approx. 1.65 V vs. RHE are reached (η = 0.42 V) a dramatic sharp increase of the anodic potential is observed. This corresponds to the OER-electrocatalyst reaching a potential region where corrosive degradation of the Ir-material via dissolution is known to occur.[36] Once 1.8 V vs. RHE (η = 0.57 V) are reached, the catalyst can be considered as deactivated as above such

potentials, degradation of the glassy carbon support of the RDE occurs.

At Ir-loadings of 50 and 100 μg_{Ir} cm^{-2}, MW-Ir/ATO proved to be the only OER-catalyst able to maintain stable overpotentials over a period of 24h, which indicates excellent performance when compared to more typical loading of 2 mg_{Ir} cm^{-2} commonly used in literature studies.[29] Even at loadings as low as 20 μg_{Ir} cm^{-2}, MW-Ir/ATO maintained rather stable potentials over 15h (Figure 2). These results compare very favorably to the amorphous AA-IrO_x benchmark, which was deactivated after only one hour at the same Ir-loading of 20 μg_{Ir} cm^{-2}. The crystalline SA-IrO_2 benchmark could not maintain j = 10 mA cm^{-2} at stable potentials. It appears that in terms of stability-related OER-performance, MW-Ir/ATO used at loadings equal to or above 50 μg_{Ir} cm^{-2} surpasses all Ir-based benchmarks reported in peer reviewed literature under similar conditions.[5, 55]. Hence it became of prime interest to determine whether an optimal compound morphology or rather the nature of the produced Ir-phase were responsible for the exceptional OER-performance.

Table 2. Benchmarking parameters for the most performant samples compared to previously reported reference compounds during a galvanostatic measurement at 10 mA cm^{-2}.

Catalyst	$\eta_{t=0}$ (V)	$\eta_{t=2h}$ (V)	$\eta_{t=24h}$ (V)	Ir-loading (μg_{Ir} cm^{-2})
MW-Ir/ATO	0.33	0.36	--[b]	20
MW-Ir/ATO	0.31	0.33	0.35	50
MW-Ir/ATO	0.31	0.32	0.34	100
AA-IrO_x	0.44	--[b]	--[b]	20
SIROF[4]	0.34	0.36	0.44	n.r.[a]
Sputtered Ru[4]	0.28	0.34	0.82	n.r.[a]
20wt.% Ir/C[22]	0.38	--	--	28
AIROF[21]	0.28	0.30	--	--

[a] Reactive sputtering resulted in a >100 nm thick Ir-film (see ref. [5, 56])

[b] Not reached as potentials overshot the 1.8 V vs. RHE-mark earlier

2.2.2. Physico-chemical characterization of MW-Ir/ATO

The XRD-pattern of the prepared MW-Ir/ATO showed only the broad rutile-type pattern of MW-ATO (Figure S4). No crystalline Ir-oxide phase could be detected. Since X-ray fluorescence spectroscopy (XRF) confirmed the successful loading of Ir on MW-ATO with a quantified loading of 33 mol.%, which is close to the target value of 30 mol.%.

Scanning Transmission Electron Microscopy (STEM).

In order to verify the successful loading of amorphous Ir-particles onto the ATO-support, the sample morphology of MW-Ir/ATO was studied using STEM. Figure 3.a) shows an annular dark-field STEM (ADF-STEM) image of MW-Ir/ATO. In ADF-STEM mode, heavy elements such as Ir appear much brighter than the Sn/Sb-containing ATO support. The combination of ADF-STEM and elemental mapping using energy dispersive X-ray spectroscopy (EDX, Figure 3.b) confirm the homogeneous loading of Ir onto the ATO-support in the form of 2-4 nm particles (Figure S6). The result is a highly nanostructured compound with S_{BET} = 154 m^2 g^{-1}. Note that some bigger spherical Ir/ATO-agglomerates could also be observed (Figure S7).

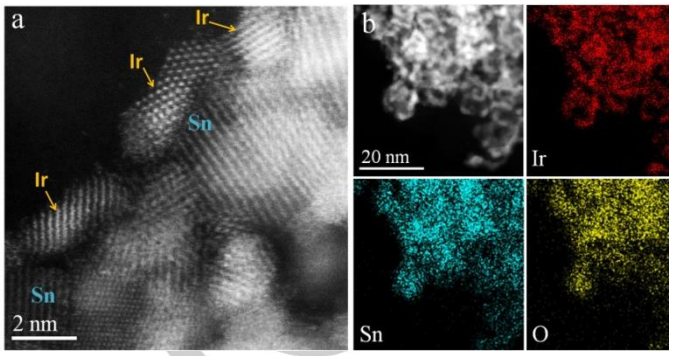

Figure 3. ADF-STEM imaging of MW-Ir/ATO with corresponding EDX-based elemental mapping. Ir is immediately reduced to Ir^0 under the electron beam.

Importantly, the amorphous Ir-phase is readily reduced under the electron beam to metallic Ir as suggested in previous reports.[37] Therefore, the interpretation of (S)TEM-imaging should be undertaken with great care. Until appropriate electron beam conditions have been found for the observation of such Ir-phases, we limit ourselves to the extraction of information about the sample morphology and Ir-distribution.

Thermogravimetric-analysis (TG)

The sample composition was determined by TG coupled with mass-spectrometry (TG-MS). The samples MW-ATO and MW-Ir/ATO were calcined in 21% O_2/Ar (100mln min^{-1}) using a 10 K min^{-1} heating ramp from room temperature to 800°C. Figure S8 shows the resulting mass loss profiles and the water evolution signals (m/z=18).

A first mass loss event observed below 150°C for both the loaded and unloaded MW-ATO-support can be attributed to the removal of weakly bound physisorbed water, which occurs at 87°C for MW-ATO and 120°C for MW-Ir/ATO, indicating a higher affinity of physisorbed water for the Ir-loaded compound. Subsequent mass loss between 150 and 500°C is to be assigned to mainly hydroxyl group decomposition as no other significant contributions are detected in MS besides traces of carbon (CO_2 evolution, 180-220°C) and NH_3 (NO removal, 420-450°C). The water resulting from hydroxyl decomposition above 150°C according to 2 M-OH → M-O-M + H_2O_{chem} is referred to as chemisorbed water. Crystalline water removed at temperatures above 150°C is neglected. The unloaded MW-ATO loses 1.4 wt.% of physisorbed water and features a late hydroxyl group decomposition in 21%-O_2/Ar with a first minor water evolution peak at 270°C and a major peak centered at around 425°C. The loss of chemisorbed water accounts for 3.3 wt.%, which is consistent with a highly hydroxylated ATO-surface typical for hydrothermally prepared compounds.

The chemisorbed water fraction in MW-ATO compares to a chemisorbed water fraction of 5 wt.% in the loaded MW-Ir/ATO. Taking into account the 26%-decrease of S_{BET} between MW/ATO and MW/Ir/ATO and the significantly higher atomic mass of Ir in MW-Ir/ATO, the higher chemisorbed water mass

fraction indicates a significantly higher molar hydroxyl fraction in the Ir-loaded compounds. It is not possible to verify wether the higher hydroxylation is to be solely attributed to the Ir-phase, however the increased molar hydroxyl-fraction is an indication of higher surface hydroxylation of the Ir-phase or even the presence of bulk hydroxyl groups. As a result, the Ir-phase of MW-Ir/ATO must be regarded as an amorphous Ir-oxohydroxide rather than a bulk oxide with a hydroxylated surface. We thus succeeded in preparing an Ir-oxide/hydroxide-type compound in line with the objective of studying the potentially superior OER-performance of such a phase. A next step was to identify the OER-relevant characteristics of such a phase.

2.2.3. Chemical environment of Ir

Mixed Ir-oxidation states have been recently highlighted as crucial to the superior OER-performance of certain Ir-phases.[39] In order to reveal Ir-species present in MW-Ir/ATO we combined temperature-programmed reduction (TPR) and X-ray photoelectron spectroscopy (XPS). These techniques are complementary methods giving respectively access to phase specific bulk reduction profiles and XPS-spectra allowing for the deconvolution of species present in the near-surface region of a compound.

Temperature-programmed reduction (TPR)

In order to detect reduction features specific to the XRD-amorphous Ir-oxohydroxide phase and determine its average oxidation state, the TPR-profiles of MW-ATO and MW-Ir/ATO resulting from a 6 K min^{-1} heating ramp in 5%-H_2/Ar were compared to AA-IrO_x and SA-IO_2. Figure S9 shows the reduction to metallic Ir and Sn. Prior to TPR, the samples were purged for at least one hour in Ar. This purge was repeated after the TPR experiment. Discrepancies between the transient H_2-signals observed before and after TPR during the switch at room temperature from Ar to a 5%-H_2/Ar-stream would indicate adsorption and/or consumption of H_2 by the sample. Neither SA-IrO_2 nor MW-ATO showed RT-H_2-adsorbtion or -consumption. In contrast, significant amounts of H_2 were taken up by MW-Ir/ATO (Figure S9). Such an observation is in line with the observation of Reier et al. that amorphous Ir-oxide/hydroxides started reducing at RT, in contrast to the more crystalline IrO_2-structures. Thus, H_2-uptake at room temperature seems to be a specific feature of the amorphous Ir-oxohydroxide phase formed under hydrothermal treatment conditions. Since no hydrogen release is detected further on in the experiment, the amount of H_2 taken up by the sample at RT has to be included into the total amount of H_2 consumed during TPR.

The H_2-TPR-profiles correspond to the H_2-consumption detected while heating the sample in a 5%-H_2/Ar flow at 6 K min^{-1}. Such characteristic profiles are useful in identifying or distinguishing oxide phases. We first analysed the TPR-profile of the bare MW-ATO (blue line, Figure S9) in order to isolate the contribution of the support. A first small reduction feature is observed at approx. 240°C while the major reduction event corresponds to a broad H_2-consumption feature centered around 593°C. Such a profile compares well with the TPR-profile of nanostructured undoped SnO_2 reported by Sasikala et al.[57]. The shift of the major reduction event to 620 °C can be explained by the more than twice as high heating ramp. The authors also observed a first reduction event at 295°C assigned to the reduction of distorted SnO_2-crystal domains on the surface of nanoparticles. This assignment of the first reduction feature can be transposed to the nanostructured MW-ATO, which probably features similar distorted ATO-domains.

The loaded MW-Ir/ATO was characterized by a sharp reduction feature at 77°C (inset in Figure S9). This compares well with the signal attributed by Reier et al. to their amorphous Ir-oxide/hydroxide phase and allows us to identify this sharp peak with the reduction of the Ir-oxohydroxide phase. Additional confirmation for this assignment comes from the similar TPR-profile reported for the pure Ir-oxohydroxide benchmark AA-IrO_x, which is close in nature to our compound. The additional feature observed at 123°C for MW-Ir/ATO is also attributed to the reduction of Ir-oxoydroxide and plausibly account for a second reduction step or morphological effects, such as the reduction of the more compact spherical structures observed in TEM (Figure S7). These two reduction features are assigned to the Ir-phase and confirm that the amorphous Ir-phase is distinct from crystalline IrO_2. Indeed the TPR-profile of SA-IrO_2 shows one main reduction peak at 239°C (purple line, Figure S9), which corresponds to the usual reduction behavior of IrO_2.[31]

The broad feature observed for MW-Ir/ATO above 250°C with peaks at 296 and 346°C is assigned to the ATO-support, which is reduced ca. 300°C below the bare MW-ATO. It seems that the Ir-loading has a dramatic effect on the reduction sensitivity of the ATO-matrix and poses the question whether the already reduced Ir-particles at the surface act as H_2-activation catalysts and/or preferential adsorption sites during TPR, thus modifying the ATO-reduction mechanism.

The detected RT-H_2-consumption and early reduction features of MW-Ir/ATO provide characteristic fingerprints of the XRD-amorphous Ir-oxohydroxide phase, in line with similar reports by Pfeifer et al.[42, 43] and Reier et al.[31] The quantification of H_2-consumption also allows determining the average oxidation state of the Ir in MW-Ir/ATO, as described in S.I, and was determined to be in a +3.28-oxidation state. Based on this value, the Ir-oxohydroxide phase is inferred to involve Ir-oxidation states of less than +IV. Based on recent literature stressing the importance of mixed oxidation state in active Ir-based OER-electrocatalysts,[39] we decided to further investigate this feature via XPS in order to verify the presence of such mixed oxidation states in the OER-relevant near-surface region of the Ir-particles.

X-ray photoelectron spectroscopy (XPS)

In order to determine which Ir-species lead to mixed oxidation state of in MW-Ir/ATO, the sample was studied using X-ray photoelectron spectroscopy (XPS). Due to the small 2-4 nm size of the Ir-particles observed in STEM (Figure 3), bulk as well as Ir-surface species contribute to the XPS-signals, which are thus an average over all Ir-species present in the sample. No contribution from metallic iridium could be detected in the Ir 4f peak at 60.9 eV[58] (Figure 4). Further analysis of the Ir 4f lineshape in order to extract chemical information about Ir-species present proved more difficult. Indeed, when studying OER-relevant Ir-based catalysts by XPS a major challenge is that even well-defined rutile IrO_2 presents an atypical Ir 4f-lineshape. The Ir 4f lines of Ir^{IV} cannot be fitted with the Doniach-Šunjic function often applicable for asymmetric core level spectra

of conductors. For this purpose, we recently developed an accurate Ir 4f fit model for rutile IrO_2 by combining theoretical calculations with experiments.[42, 43] Within a one-electron picture we found that Gaussian "shake-up" satellites add intensity to the Ir 4f spectrum 1 and 3 eV above the main lines. This model gives more solid ground for the identification of the contributions of Ir^{IV}-species to Ir 4f spectra and allows for a precise Ir 4f deconvolution in order to identify contributions from other Ir-oxidation states.

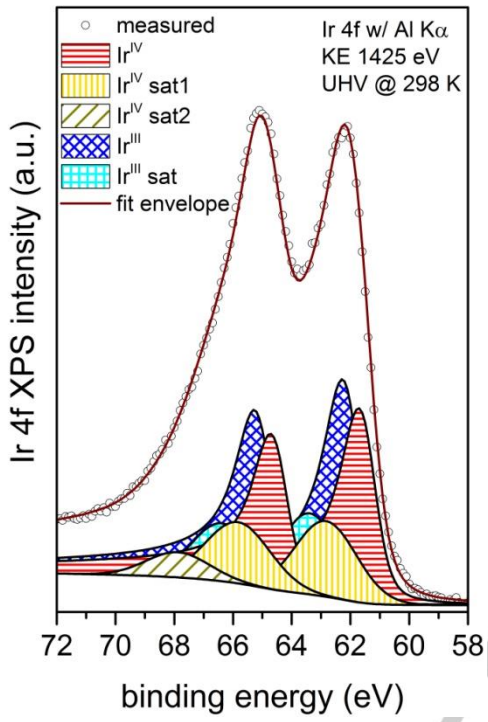

Figure 4. XPS-measurement of the MW-Ir/ATO in the Ir4f-region using an Al-Kα-source at 1425 eV and fitted using the models developed by Pfeifer et al.[42, 43]

It was already noted in several studies on Ir-based OER-catalysts performed ex-situ[31] as well as in-situ[59] that OER-active compounds presented additional contributions in their Ir4f-spectra at higher binding energies than expected for Ir^{IV} (61.8 eV for $Ir4f_{7/2}$) and 64.8 eV for $Ir4f_{5/2}$). Based on the higher binding energies of the Ir4f-electrons of the additional species, Casalongue et al. attributed these contributions to Ir^{V}-species formed in-situ during the OER and involved in the catalysis of water oxidation.[59] However, caution should be used when assigning oxidation states based only on binding energy (BE) shifts. Shifts to higher binding energies are usually associated with higher oxidation states, but the oxidation state is not the only factor influencing the BE. *E.g.* in the case of silver, the BE of AgO shifts to lower BE than the metal due to final state effects.[60] This shows that in certain cases lower oxidation states can appear at higher BE. In order to establish an accurate description of the electronic structure of Ir oxides, in our aforementioned study we investigated the origin of contributions to the XPS- and NEXAFS-spectra of amorphous Ir-oxides with TPR-derived oxidation states below +IV.[42, 43] The developed model shows that Ir 4f-intensity observed at higher binding energies than Ir^{IV} in amorphous Ir-oxohydroxide samples could be attributed to Ir^{III}-species. This model was used to fit the XPS data recorded for MW-Ir/ATO in the Ir4f-region (Figure 4). The obtained fit describes the experimental data accurately and confirms that the near-surface region of the Ir-particles probed at kinetic energies of 1425 eV consists of a mixed valence state $Ir^{III/IV}$-compound. Ir^{III}-species accounted for more than 50% of the observed intensity, which is well in line with the average $Ir^{3.28}$-oxidation state calculated from the TPR-results.

2.3 Identification of OER-relevant features: the effect of thermal treatment on MW-Ir/ATO

The characterization of MW-Ir/ATO revealed an ATO-supported $Ir^{III/IV}$-oxohydroxide with outstanding OER-performance. In order to determine to what extent the nature of the Ir-phase is responsible for the OER-performance, rather than morphological effects, a strategy of gradual alteration to the Ir-phase and observation of the resulting effect on OER-performance was pursued. For this purpose, MW-Ir/ATO was subjected to careful thermal treatment at 250°C and 350°C under both inert (Ar) and oxidative (21% O_2/Ar)-streams, resulting in four compounds labeled as follows: Ir_(250/350)_(Ar/O_2) (see Table 1). Such moderate conditions were chosen in order to mostly affect the Ir-phase and avoid major changes to the morphology as exemplified by Reier et al.[31] The temperature range was chosen based on TGMS (Figure S8), which revealed that important dehydroxylation of MW-Ir/ATO starts early on in the 150-200°C temperature range. Thus changes in the OER-performance of the resulting compounds can be related to structural changes such as dehydroxylation, oxidation/reduction and crystallization, and eventually lead to the identification of OER-relevant fingerprints.

2.3.1. Effect of thermal treatment on OER-performance

In order to assess the effect of thermal treatment on the OER-performance of the Ir-phase, a systematic electrochemical protocol was designed for the comparative testing of MW-Ir/ATO and Ir_(250/350)_(O_2/Ar). The OER-activity was assessed via linear sweep voltammetry (LSV). For easier comparison, we report the loading-dependent mass activity of the iridium-catalysts at a typical overpotential of η = 0.35 V (Figure S12).[55] In order to improve the statistical relevance of the results, the test protocol was repeated for each compound with three different loadings (20, 50 and 100 μg_{Ir} cm^{-2}). In order to assess the stability of the compounds under OER-conditions, the mass activities before and after a CP-based 2h-stability test at 10 mA cm^{-2} are compared. Figure 5 shows a summary of these values obtained for the different loadings of each compound before (plain bars) and after the stability test (dashed bars). Similar mass activities before and after the CP-step indicate a stable catalyst whereas loss of mass activity indicates deactivation.

We first considered the initial mass activities of all compounds (plain bars in Figure 5). It appears that the mass activity gradually decreases with increasing Ir-loading, which suggests that utilization effects come into play. A build-up of Ir-layers and decreasing Ir-utilization is to be expected from a drop-coating procedure such as ours. The comparison of initial activities shows that the untreated MW-Ir/ATO is the most active electrocatalyst, with mass activities reaching 1.86 A mg_{Ir}^{-1} at η=0.35 V for the lowest loading of 20 μg_{Ir} cm^{-2}.

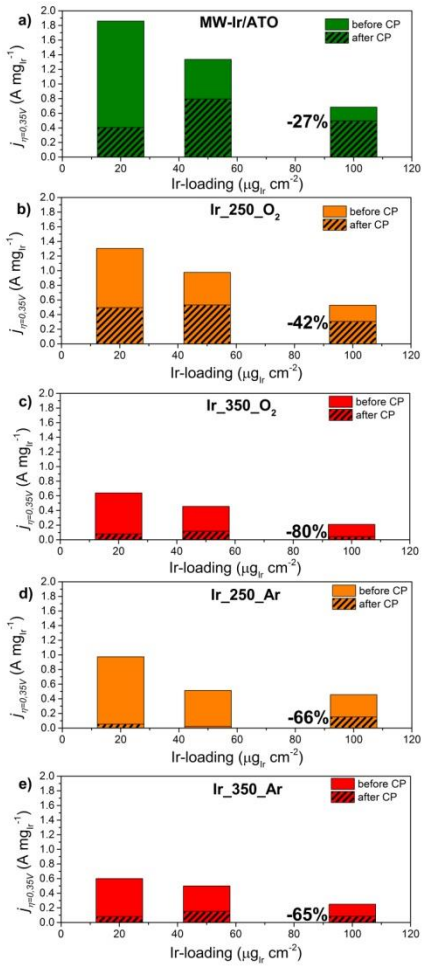

Figure 5. Loading-dependent mass activity at η=0,35 V before (plain bars) and after CP at 10 mA cm^{-2} (patterned bars) for (a) MW-Ir/ATO (a) and its thermally treated products (b) Ir_250_O_2, (c) Ir_350_O_2, (d) Ir_250_Ar and (e) Ir_350_Ar. The relative changes in mass activities at 100 μg_{Ir} cm^{-2} are indicated for each compound on the left of the corresponding bar.

For all compounds the best initial mass activitiy was reported for the lowest Ir-loading, showing that dispersion on the electrode and Ir-utilization was best under these conditions. When considering the thermally treated samples, a substantial decrease in initial mass activities was observed independently of the gas atmosphere used during the treatment. For the 250°C-treated samples the mass activity decreased by at least 23% for Ir_250_O_2 and at least 33% for Ir_250_Ar. An even more pronounced depletion was observed for the 350°C-treated samples. Compared to MW-Ir/ATO, the initial mass activity of Ir_350_O_2 decreased by 65%. For Ir_350_Ar a loss of at least 63% of mass activity was observed. Obviously, especially the treatment in dry atmospheres at 350°C profoundly affected the initial OER-activity of the thermally treated samples.

After comparing the initial mass activities of the samples, the stability of the catalysts was assessed by comparing the mass activities before and after the 2h-CP test performed at 10 mA cm^{-2}. This current density allows us to compare our data with peer reviewed literature and to minimize the so called bubble blockage effects of the electrode. The study of the CP-curves (see Figure S13) showed that the samples are deactivated following different regimes, depending on the anode potential region. As in the CP-tests performed on MW-Ir/ATO (Figure 2), 1.65 V vs. RHE constitute a threshold above which Ir-dissolution via corrosive processes leads to fast deactivation of the OER-catalyst.[36, 61] In the case of Ir-loadings of 20 μg_{Ir} cm^{-2}, several samples reached this threshold before the end of the 2h-CP test (Figure S13). This means that strong corrosive degradation contributed to catalyst deactivation, explaining the especially sharp deactivations observed at these loadings. Comparison of stabilities would thus be complicated by the fact that some compounds had seen potentials above 1.65 V vs. RHE and others not. In order to simplify the comparison, we chose to compare the mass activities of the five compounds for 100 μg_{Ir} cm^{-2}. Indeed at such a loading none of the CP-curves (Figure S13) showed the sharp potential increase characteristic of fast corrosive degradation.

The final OER-activities (dashed bars in Figure 5) seem to rank following the same order as initially: MW-Ir/ATO is still the most active compound, having lost only 27% of mass activity, followed by Ir_250_O_2. Ir_250_Ar and the 350°C-calcined samples exhibit the lowest activities and have thus been deactivated the most. A striking difference can be observed between the two samples calcined at 250°C: Despite similar initial activities, Ir_250_O_2 lost only 42% mass activity, while Ir_250_Ar lost 66% mass activity and exhibits fast corrosive deactivation for 20 and 50 μg_{Ir} cm^{-2} (see Figure S13). This indicates that the Ar-treatment at 250°C much more adversely affected the stability of the Ir-phase under OER-conditions. The identification of structural features are more affected in Ir_250_Ar than in Ir_250_O_2 might thus allow to isolate OER-relevant features of the initial MW-Ir/ATO. Treatment at 350°C had an even greater impact on the stability. Mass activities decreased by 80% for Ir_350_O_2 and by 65% for Ir_350_Ar. As a result an inverse tendency appears, where the Ar-treatment didn't further worsen the stability of the Ir_350_Ar in comparison with Ir_250_Ar. Ir_350_O_2 on the other hand exhibited twice the mass activity loss after CP when compared to Ir_250_O_2. In order to relate the observed differences in OER-performance to morphological and structural changes, we thoroughly characterized the thermally treated samples via a multi-analytical approach based on the characterization of MW-Ir/ATO described in section 2.2.

2.3.2. Structural investigation

The XRD-patterns of the thermally treated samples only revealed the rutile-type pattern of the ATO support (see Figure S4). No crystalline phase could be identified, which indicates that no large Ir-crystallites were formed independent of the temperature or gas flow used. The thermal treatment had little effect on S_{BET} at 250°C, with a minor 10% decrease observed after Ar- and 21%-O_2/Ar-treatment (Table 3). Such minor changes are a first indication that the morphology of Ir-phase was little affected at 250°C and that differences observed in the OER-performance of MW-Ir/ATO, Ir_250_O_2 and Ir_250_Ar were linked to changes in the nature of the OER-active Ir-phase. After treatment at 350°C, a more pronounced diminution in S_{BET} of approx. 30% was observed in both atmospheres (Table 3). Again however, morphological changes alone cannot explain the over 63% decrease in initial OER-activity when comparing Ir_350_O_2 and Ir_350_Ar to MW- Ir/ATO.

Table 3. Specific surface areas of MW-Ir/ATO and thermally treated products

Electrocatalyst	S_{BET} ($m^2\ g^{-1}$)
MW-Ir/ATO	154
Ir_250_O_2	140
Ir_350_O_2	105
Ir_250_Ar	144
Ir_350_Ar	109

STEM

In order to verify that the morphology of Ir-loaded ATO was not dramatically affected by the thermal treatments and could only be held partly accountable for the changes in OER-performance, Ir_250_O_2 and Ir_350_O_2 were studied using STEM and compared to MW-Ir/ATO. The ADF-STEM-imaging of Ir_250_O_2 (Figure 6.a) revealed a similar morphology to MW-Ir/ATO (Figure 3 and S6) with bright metallic Ir-particles of approx. 2-4 nm homogenoously dispersed in the ATO-support. The observation of metallic Ir indicates that the Ir-phase was immediately reduced by the electron beam, much as for MW-Ir/ATO. The observed structure confirms that no major changes in sample morphology occur upon thermal treatment at 250°C, as shown by the little change in S_{BET}. We extrapolate this observation to Ir_250_Ar due to the even more stable S_{BET} (-6%, Table 3).

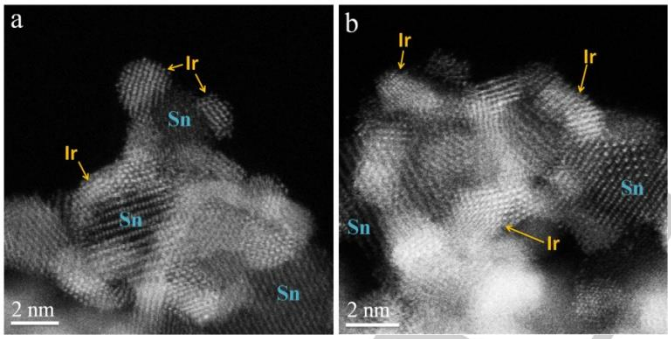

Figure 6. ADF-STEM imaging of Ir_250_O_2 (a) and Ir_350_O_2 (b). Ir is immediately reduced to Ir^0 under the electron beam.

For Ir_350_O_2, the morphology was found to differ from MW-Ir/ATO and Ir_250_O_2. Ir-particles seemed larger (brighter spots correspond to larger Ir-aggregates) and showed a higher wetting on the ATO-support (Figure 6.b). This is in line with the more important 30%-decrease observed in the S_{BET} of Ir_350_O_2. Nonetheless, the Ir-particles remain highly disperse and nanostructured, indicating that sintering phenomena are limited and cannot entirely explain the 65% decrease observed in the initial mass activity of Ir_350_O_2. A first hint about the nature of the Ir-phase in Ir_350_O_2 was derived from time-resolved STEM-imaging. In some spots small rutile-IrO_2-domains were stable long enough to be observed before they were reduced to metallic Ir (Figure S14). This suggests that Ir_250_O_2 featured a highly beam sensitive Ir-phase similar to MW-Ir/ATO, whereas more beam-stable IrO_2 was formed in Ir_350_O_2. In order to confirm this conjecture and understand the case of the Ar-treated samples, we then resorted to TG and TPR.

TG-analysis

In order to simulate the effect of thermal treatment on MW-Ir/ATO, the preparation of Ir_250/350_O_2_Ar was simulated in a stepwise TG-experiment were MW-Ir/ATO was treated in two consecutive steps at 250°C and 350°C for 1h in 21%-O_2/Ar or Ar (100mln min^{-1}). The resulting mass loss profiles are shown in Figure S15. It can be observed that after 1h at 250°C, MW-Ir/ATO loses 0.33% more mass in Ar-stream than in oxidative stream. As dehydroxylation of MW-ATO occurs at higher temperatures (Figure S8) and XRD reveals no reduced Sn or Sb after the experiment, the mass change is related to the Ir-phase. If one neglects other stream-dependent mass changes such as reduction in Ar, or oxidation in 21%-O_2/Ar at 250°C, this indicates that a higher amount of the hydroxyl-fraction attributed to the Ir-oxohydroxide phase is lost after annealing MW-Ir/ATO at 250°C in Ar compared to the behavior in oxidative stream.

TPR

The nature of the thermally induced transformations could be further understood by studying the behavior of the samples under a reducing 5%-H_2/Ar-stream as in the TPR-experiment described in Section 2.2.3. A first distinctive feature assigned to the amorphous $Ir^{III/IV}$-oxohydroxide-phase in MW-Ir/ATO was the important RT-H_2-uptake. When examining the RT-H_2-uptake of Ir_250/350_O_2/Ar, it appeared that Ir_250_Ar and Ir_250_O_2 both absorbed amounts of H_2 comparable to MW-Ir/ATO (Table 4). This indicates that the Ir-phase of the samples calcined at 250°C is still close in nature to MW-Ir/ATO. For Ir_350_Ar and Ir_350_O_2, the amount of RT-adsorbed hydrogen clearly diminished, indicating that the Ir-phase, not able to absorbe H_2 at room temperature. is being formed. This observation goes in line with the properties of crystalline IrO_2, as shown for SA-IrO_2 (Table 4).

Since the TPR-profile is specific to oxidic phases present in a sample, we analyzed the TPR-profiles of Ir_250/350_O_2/Ar in order to gather more indications on the thermally-induced transformations of the Ir-phase. In Figure 7, the TPR-profiles of the samples produced at 250°C (Figure 7.a) and 350°C (Figure 7.b) were compared to MW-Ir/ATO (green profiles).The features assigned to ATO-reduction above 250°C remain relatively stable independently of the thermal treatment, indicating that the bulk electronic structure of the ATO-support was little affected. On the other hand, important differences in the reduction profiles assigned to Ir were observed. The TPR of MW-Ir/ATO (section 2.2.3) allowed us to identify the sharp reduction peak at 77°C as a characteristic reduction feature of $Ir^{III/IV}$-oxohydroxides (Figure S9). At 250°C (Figure 7.a)), changes are subtle: The sharp feature at 77°C only slightly diminishes for both Ir_250_O_2 and Ir_250_Ar (inset in Figure 7.a), indicating a minor depletion in the Ir-oxohydroxide phase. For Ir_250_Ar, the characteristic peak also shifted from 77 to 75°C hinting at a slightly higher reducibility of the amorphous Ir-oxohydroxide phase upon thermal treatment. In both atmospheres, a slightly higher amount of the species reducing at 123°C seems to be formed, which

might be attributed to morphological changes such as slightly bigger Ir-particles.

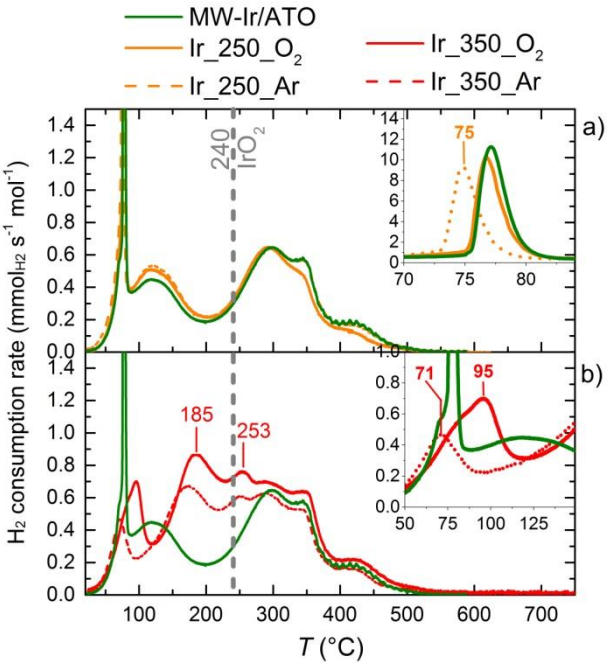

Figure 7. TPR-profiles of MW-Ir/ATO (green line), and the samples obtained after treating MW-Ir/ATO in 21%-O_2/Ar (full lines) and Ar (dotted lines) at 250°C (a, orange) and 350°C (b, red). The H_2-consumption rate is normalized by the mass of sample not including the physisorbed water fraction.

The H_2-consumption was used to calculate average oxidation states (see S.I.). The result showed no significant difference between Ir_250_O_2 and Ir_250_Ar (see Table 4). However it seems that the dehydroxylation observed in TG goes along with a slight reduction of MW-Ir/ATO from +3.28 to approx. +3.00 in both atmospheres. The fact that the average oxidation state of Ir_250_O_2 is even lower than for Ir_250_Ar shows that the higher mass loss observed in TG (Figure S15) is not related to higher O_2-release but rather to more pronounced dehydroxylation in Ar. This higher loss of hydroxyl groups is the only feature distinguishing Ir_250_Ar from Ir_250_O_2 so far, despite the so vastly different stabilities under exhibited OER-conditions. This leads us to the conclusion that the hydroxyl groups in the $Ir^{III/IV}$-oxohydroxide phase are a key feature in understanding the outstanding OER-performance of MW-Ir/ATO.

Just as for the RT-H_2-uptake, the most significant changes of the Ir-phase are shown by TPR-profiles of the samples treated at 350°C (Figure 7.b). Both Ir_350_O_2 and Ir_350_Ar exhibit two additional reduction peaks centered at 185 and 253°C, which is in close range of the IrO_2-reduction feature obtained for SA-IrO_2 at 239°C. This suggests that oxidic Ir-phases close in nature to IrO2 have been formed in both compounds. Therewhile, the sharp features below 100°C have been significantly reduced in both samples, showing the disappearance of the Ir-oxohydroxide phase. The inset in Figure 7.b shows that only a small residual reduction peak appears for Ir_350_Ar at 71°C, while a broader and more intense is detected for Ir_350_O_2 at 95°C.

Table 4. Characteristic values extracted from TPR-profiles including the mol of compound-normalized H_2-uptake at room temperature ($n_{H2,RT}$), the H_2-consumption during TPR ($n_{H2,TPR}$) and the resulting calculated average oxidation state of Ir.

Compound	$n_{H2,RT}$ (mmol mol^{-1})	$n_{H2,TPR}$ (mmol mol^{-1})	Avgerage Ir-oxidation state
MW-Ir/ATO	185	1698	3.28
Ir_250_O_2	215	1593	2.9
Ir_350_O_2	67	1964	4.06
Ir_250_Ar	201	1636	3.00
Ir_350_Ar	110	1645	2.52
SA-IrO_2	0	2040	4.08

The different peak intensities observed for Ir_350_O_2 and Ir_350_Ar reflect different total H_2-consumption of the samples and result in significantly different calculated average oxidation states. Ir_350_Ar was found to be in an average $Ir^{+2.52}$-state, indicating a partial reduction of the sample to oxidation states below +III, which suggests the formation of metallic Ir since oxidic Ir^{I}- and Ir^{II}-species have not been reported under standard (*P*,*T*)-conditions. Ir_350_O_2 was found to be $Ir^{+4.06}$. This indicates that the Ir-phase is mostly transformed into an IrO_2-type phase in under oxidative conditions at 350°C.

The suspected formation of crystalline IrO_2 at 350°C in both atmospheres goes along with the sharp reduction of initial OER-mass-activity and confirms the adverse effect of transforming amorphous Ir-oxohydroxide phases into crystalline IrO_2 as already suggested by Reier et al.[31] The partial reduction to metallic Ir in Ar at 350°C might explain the slightly higher apparent mass activity of Ir_350_Ar. The re-oxidation of the metallic Ir at OER-potentials is suggested to contribute to the observed current density, thus lowering the required overpotentials. At 250°C in both atmospheres, the reduction behavior of the amorphous Ir-phase seems to be less affected, indicating that it remains close in nature to MW-Ir/ATO. The dominating effect appears to be the stronger dehydroxylation observed in Ar-atmosphere via TG-analysis and highlights the possible role of hydroxyl groups for stabilizing the electrocatalyst under OER-conditions. This observation is in line with OER-relevant surface hydroxyls groups described recently by Reier et al. in a series of Ir/Ni-mixed oxides.[30]

Raman analysis

In order to confirm the formation of a less active IrO_2-type phase at 350°C, the samples were studied via Raman spectroscopy. In order to analyze the spectra, literature references were used.[62, 63] We first identified the contributions from MW-ATO (black spectrum in Figure 8). For crystalline SnO_2, the three expected observable Raman modes E_g (476 cm^{-1}), A_{1g} (629 cm^{-1}), and B_{2g} (772 cm^{-1}) can be detected in the spectrum of MW-ATO (black line in Figure 8).[63] Additional broad features, for instance at 570 cm^{-1} are assigned to surface Raman modes that cannot be

neglected for small nanoparticles exhibiting distorted crystal structures towards the surface[64], as in the case of our MW-ATO.

In MW-Ir/ATO (green line), the most prominent feature appears at 493 cm^{-1}, which is clearly distinct from the observable E_g-, A_{1g}- and B_{2g}-Raman modes of rutile-IrO_2 (dashed lines in Figure 8).[62] The Raman signature of the ATO-support is identified by two broad shoulders above 600 cm^{-1}. Deconvolution of the spectra is ambiguous because of the strongly overlapping broad features. However, we can assign the most prominent new feature at 493 cm^{-1} to the $Ir^{III/IV}$-oxohydroxide.

Recently some studies described planar bis-μ-oxo di-Ir(IV) structures involved in the structure of active Ir-based catalysts formed from organometallic precursors under OER-relevant conditions.[65, 66] Hintermair et al. calculated the corresponding Raman-active vibrations and observed the Raman features of the bis-μ-oxo di-Ir(IV)-unit in-situ between 559 and 666 cm^{-1}.[65] Our main peak at 493 cm^{-1} is shifted compared to these values and smaller contributions cannot be distinguished from the complex ATO-signal. However, Huang et al. pointed out the relevance of such iridium-oxo-domains for the understanding of OER-relevant amorphous iridium-oxohydroxide-based catalysts. The characteristic peak observed at 493 cm^{-1} for MW-Ir/ATO might be assigned precisely to such an amorphous Ir-oxo-domain.

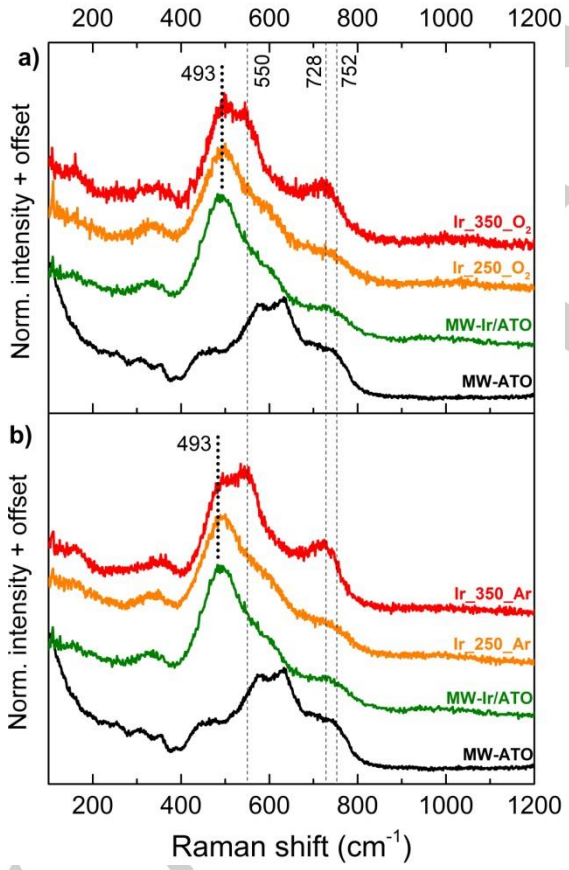

Figure 8. Raman spectra of the support (MW-ATO), of the as prepared MW-Ir/ATO as well as after thermal treatment at 250 or 350°C in 21%O_2/Ar (a) or 100% Ar (b). The observable Raman modes of IrO_2 according to [38a] are indicated as grey dashed lines, the dark dotted line indicates the feature at 493 cm^{-1} attributed to Ir-oxohydroxide.

The effect of thermal treatment on MW-Ir/ATO is clearly reflected in the Raman spectra recorded for the samples calcined at 350°C in 21%-O_2/Ar and 100%-Ar. Distinct additional contributions appear for Ir_350_O_2 and Ir_350_Ar at 550 cm^{-1} as well as around 730 cm^{-1}. These features can be attributed to the E_g-, A_{1g}- and B_{2g}-modes of IrO_2-rutile and confirm the formation of an IrO_2-type phase as indicated by the TPR-profile. It is also apparent that the ratio between the IrO_2-peak at 550 cm^{-1} and the Ir-oxohydroxide-peak at 493 cm^{-1} are shifted in opposite directions for Ir_350_O_2 and Ir_350_Ar. For Ir_350_O_2, the 493 cm^{-1}-feature is more intense than the IrO_2-E_g-peak (Figure 8.a), while the opposite trend is observed for Ir_350_Ar (Figure 8.b). This is in line with the observation the TPR-signature of the Ir-oxohydroxide was smaller in Ir_350_Ar, indicating that the amorphous Ir-oxohydroxide was decomposed faster in 100% Ar than in 21% O_2/Ar. For the samples prepared at 250°C, no IrO_2-features could be distinguished, indicating that the partially dehydroxylated amorphous Ir-oxohydroxide was still the majority phase. These observations confirm the interpretation of the TPR-profiles and the assigned transformations of the Ir-phase.

Temperature-dependent DRIFTS

In a last step, we aimed at a better understanding of the dehydroxylation process upon thermal treatment. In order to obtain fingerprints of chemical bonds present in the samples, vibrational spectroscopy was required. The use of diffuse reflectance infrared Fourier transformed spectroscopy (DRIFTS) allows for the study of compounds in a loose, powdered state under gas streams and conditions close to the real thermal treatment. Structural changes during the calcination of MW-ATO and MW-Ir/ATO in 21%O_2/Ar were studied in-situ using DRIFTS during a stepwise heating experiment to 350°C.

The DRIFTS spectra recorded for the MW-ATO support during the stepwise heating experiment are discussed in further detail in the S.I. (Figure S14). The most prominent structural features are located below 1500 cm^{-1}. A strong signal is located at 760 cm^{-1} and shifts to 778 cm^{-1} above 250 cm^{-1}, while its intensity gradually increases. According to the TGMS-profile (see Figure S8), above 250°C, MW-ATO is being strongly dehydroxylated and thus forms more oxide-like structures, leading to a sharp increase in the corresponding feature between 760 and 778 cm^{-1} (see S.I. for further detail).

The DRIFTS spectra of MW-Ir/ATO recorded at different temperatures under 21%-O_2/Ar show how the thermal treatment affected the hydroxylation of the compound. Figure 9 shows the Kubelka-Munk-corrected DRIFTS-spectra obtained after treatment to or above 100°C in 21%-O_2/Ar. According to TGMS-results, loosely physisorbed water has been removed after heating at 125°C and shouldn't contribute to the observed signal. Broad but pronounced features are observed in the 3000-3700 cm^{-1}-region, which indicates a high hydroxyl-fraction in the Ir-oxohydroxide phase (Figure 9.a). Such features indicating a highly hydroxylated nature were recently reported by Ito et al. for Ir-oxide films sputtered in a reactive wet atmosphere.[67] Contributions from hydroxyl groups at 3700-3450 cm^{-1} usually correspond to isolated OH-groups on the oxide surface, while the broad features in the 3400-3100 cm^{-1} region should be assigned to water molecules present in the bulk and strongly physisorbed on the surface as well as H-bound hydroxyl groups.

A broad feature around 2950 cm^{-1} is assigned to C-H-stretching frequencies and might originate from C-contaminations during atmospheric exposure. Such features were also observed by Ito et al. but assigned to H-bonded OH-groups.

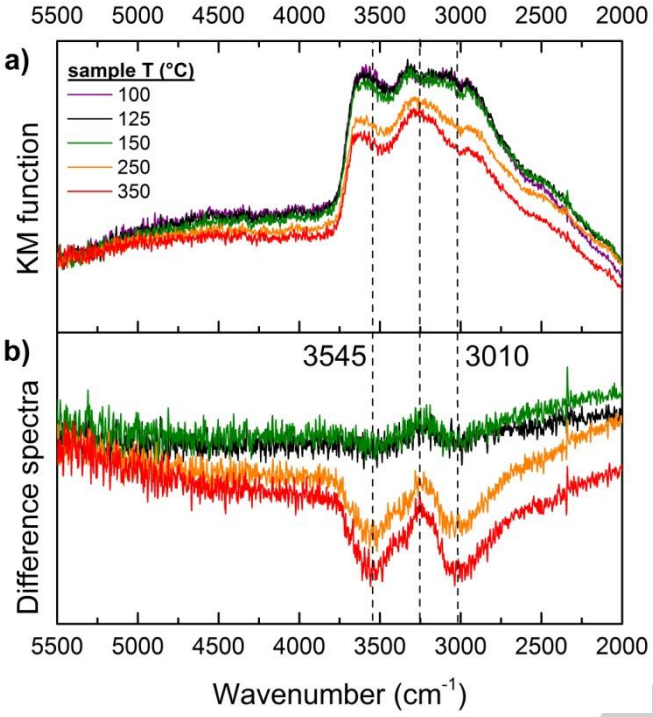

Figure 9. DRIFTS measurements (5500-2000 cm^{-1}) of MW-Ir/ATO during stepwise treatment at various temperatures in 21%-O_2/Ar, 100 mln min^{-1}. Kubelka-Munck transformation of the reflectance spectra (a) and corresponding difference spectra between said temperature and 100°C (b).

The effect of thermal treatment on the chemisorbed water fingerprint is evidenced when assessing the difference spectra between the DRIFTS recorded at a given temperature and the 100°C-spectra (Figure 9.b). Temperature-induced changes in the background scattering might account for overall baseline shifts, however two pronounced events can be isolated. At 250 and 350°C the spectra lose important contributions centered at 3545 cm^{-1} and 3010 cm^{-1}. The contribution at 3545 cm^{-1} can be assigned to isolated surface hydroxyls. As a result, the Ir-surface seems to be strongly dehydroxylated above 250°C, while H-bonded hydroxyl groups accounting for contributions above 3545 cm^{-1}, probably located deeper in the bulk, remain stable and will be removed at higher temperatures. The signal loss at 3010 cm^{-1} would in turn be assigned to the removal of surface carbonaceous species. Unfortunately, signals were too broad to be used in a comparison of the dehydroxylation of MW-Ir/ATO in oxidative and inert atmosphere. Hence, we don't discuss DRIFTS-results for Ar-calcination here.

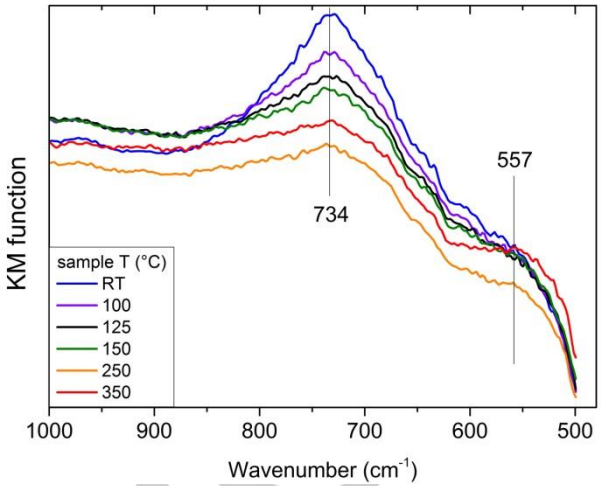

Figure 10. DRIFTS measurement of MW-Ir/ATO (Kubelka-Munck transformation, 1000-500 cm^{-1}) during stepwise treatment at various temperatures in 21%-O_2/Ar, 100mln min^{-1}.

Additional information on the effect of thermal treatment can be found at lower wave numbers. Figure 10 shows the only feature that could be clearly assigned to the ATO-support. It corresponds to the strongest feature detected for MW-ATO at 760 cm^{-1} at room temperature (Figure S16). This feature is shifted to 734 cm^{-1} in MW-Ir/ATO and instead of increasing in intensity with rising temperatures, it gradually diminishes. We suggest that the higher wetting of oxidic Ir-particles observed in STEM (Figure 6.b) is responsible for the diminution of the only clearly visible ATO-feature. Since the Ir-oxohydroxide particles are being transformed into a layer of more IR-reflective[68] IrO_2, this creates increased shielding of the ATO-support from the incident IR-radiation, thus a decreased contribution of the support to the overall spectrum. The formation of an IrO_2-type phase is confirmed by an additional shoulder visible at approx. 557 cm^{-1} (Figure 10). Indeed absorption at around 550 cm^{-1} has been repeatedly attributed in the literature to lattice Ir-O-bonds in IrO_2.[67, 69] This indicates that small crystalline IrO_2-domains even start forming at 250°C, however the absence of characteristic contributions in TPR and Raman spectroscopy for the 250°C-treated samples indicate that such IrO_2-domain still represent a minority phase.

DRIFTS of MW-Ir/ATO confirms the strong dehydroxylation of MW-Ir/ATO upon heating. It appears that the removal of OH-groups corresponding to the 3545 cm^{-1}-contribution is concomitant with the loss of OER-performance. As a result, the OH-groups appearing at 3545 cm^{-1} are suggested to be involved in the structure of the active sites precursors accommodated by MW-Ir/ATO within the $Ir^{III/IV}$-oxohydroxide matrix. They are lost once IrO_2 begins to form. Such an observation is in line with the OER-relevant reactive OH-groups recently highlighted by Reier et al.[30] and deserves further attention to determine the exact nature of these OH-species.

3. Conclusions

The reported study of hydrothermally prepared Ir-particles dispersed on ATO confirms the prominent role of the little investigated class of XRD-amorphous Ir-oxohydroxide compounds. The 30 mol.%-Ir/ATO (MW-Ir/ATO) obtained via MW-supported hydrothermal synthesis showed exceptional OER-performance under commercially relevant conditions in comparison with reported benchmarks. Careful analysis based on TGMS, TPR and XPS adapted to our purpose revealed the $Ir^{III/IV}$-oxohydroxide nature of the Ir-phase. The detrimental effect of thermal treatment highlighted that the particular chemical nature of the $Ir^{III/IV}$-oxohydroxide phase is paramount for the high activity and stability, rather than optimized particle dispersion. The appearance of small crystalline IrO_2-domains upon heating was met with a sharp decrease in OER-performance which confirms the superior electrocatalytic properties of amorphous $Ir^{III/IV}$-oxohydroxides structures for OER-electrocatalysis. We also observed that activity-relevant hydroxyl groups were removed at 250°C, faster in inert than in oxidative atmosphere. This led to a sharper decrease in OER-performance for the Ar-treated, more strongly dehydroxylated sample, highlighting the relevance of Ir-bound hydroxyls for the OER-performance.

Our proposed MW-supported synthesis pathway gives access to synthesis conditions that bridge the gap between low-temperature hydrolysis of Ir-precursors and high-temperature calcination routes. The resulting $Ir^{III/IV}$-oxohydroxide compounds bypass the conundrum of having to sacrifice activity for stability by producing crystalline IrO_2-phases.. In order to obtain a more thorough understanding of the Ir-oxohydroxide phase without the influence of support-effects, follow-up work will focus on unsupported amorphous Ir-oxohydroxides in order to gain deeper insight into OER-relevant species hosted by the $Ir^{III/IV}$-oxohydroxide structure.

4. Experimental section

4.1 ATO synthesis

Antimony-doped tin oxide (ATO) was obtained from $SnCl_4*5H_2O$ (Sigma Aldrich) and $SbCl_3$ (Sigma Aldrich) dissolved in a 95:5 molar ratio in a 0,5%-HCl/H_2O solution. The metal chloride solution was added to 200mL H_2O under constant stirring at a speed of 5g.min^{-1} using an automated laboratory reactor system (Mettler-Toledo, Labmax). During addition, reactor-pH was automatically maintained at pH=4 using 1%-NH_3/H_2O. During addition, the solution was maintained at 50°C and further aged for 1h at 50°C. The resulting colloidal suspension was subjected to hydrothermal treatment in a microwave synthesis reactor (Multiwave PRO, Anton Paar). 50mL of solution are poured into an 80mL-quartz vessel and four such vessels at a time are heated at 290°C for 1h in the microwave (ramp : 10 K min^{-1}). The product changed color from cream white to blue, typical for ATO. The vessel content was centrifuged at 5000 rpm for 10 min, redissolved in micropore-filtered water and re-centrifuged until the conductivity of the supernatant was below 0.05 mS cm^{-1}. The solid product was then dried at 80°C for 12h and ground in a mortar.

4.2 Resisitivity

For the purpose of measuring resistivities, ATO-powders were pressed as 13 mm-pellets of thickness below 1μm using a pressing dye at 7 tons for 5 min. The four-point-probe-measurement head consisted of four 2mm-spaced gold tips mounted in a row. The two outer tips were coupled to a DC precision current source Keithley 6220, whereas potential differences between the two inner tips were measured using a Keithley 6514 electrometer. The resulting apparent resistance was converted to sheet resistance taking into account the finite pellet dimensions using the geometry correction factors provided by Smits.[70]

4.3 Ir-loading of ATO

The ATO-support was then loaded with OER-active Ir. For this purpose, 310 mg of MW-ATO was added to a 100 mL-PTFE-vessel. The vessel was then filled with 62 mL H_2O containing 425.5 mg dissolved K_2IrCl_6 (Alfa Aesar, kept under Ar) under constant stirring. The pH of the resulting suspension was slowly adjusted to pH=13 using a 1M NaOH-solution. The pH was maintained for 30 min at pH=13 under constant stirring. The mixture was then allowed to age for an hour under gentle shaking. Four such vessels were then placed in the microwave synthesis reactor and heated up to 250°C using a 10 K.min^{-1} ramp under constant agitation provided by magnetic PTFE-stirrers. The temperature was maintained at 250°C for 1h. The resulting black product was centrifuged at 8000rpm for 10 min, redissolved in micropore-filtered water and re-centrifuged until the conductivity of the supernatant was below 0.05 mS cm^{-1}. The solid product was then dried at 80°C for 12h and ground in a mortar.

4.4 XRD

X-ray powder diffraction (XRD) measurements were performed on a STOE STADI-P transmission diffractometer equipped with a primary focusing germanium monochromator (Cu Kα1 radiation) and a linear position sensitive detector. The samples were mounted in the form of small amounts of powder sandwiched between two layers of polyacetate film and fixed with a small amount of X-ray amorphous grease.

4.5 BET

The surface area determination was carried out in a volumetric N_2-physisorption setup (Autosorb-6-B, Quantachrome) at the temperature of liquid nitrogen. The sample was degassed in dynamic vacuum at a temperature of 80°C for 2 h prior to adsorption. Full adsorption and desorption isotherms were measured. The linear range of the adsorption isotherm (p/p0 = 0.05-0.3) was considered to calculate the specific surface area according to the BET-method.

4.6 DR-UV-Vis

Diffuse reflectance UV-Vis spectra of ATO-powders were measured using a Agilent Technologies Cary 5000 UV-Vis_NIR spectrometer equipped with a Harrick diffuse reflectance attachment. Spectra were recorded at room temperature. The Kubelka–Munk function F(R) was used to convert diffuse reflectance data into absorption spectra using BaSO4 as white standard. Sample powders were diluted 1:10 with BaSO4 due to strong absorption features.

4.7 Thermogravimetric analysis

Thermogravimetric anaylsis (TGA), differential scanning calorimetry (DSC) and evolved gas analysis of the decomposition reaction of the samples under a 21%-O_2/Ar- or 100%-Ar-stream (100 mln.min^{-1}, 10 K min^{-1}, 800°C) were performed on a Netzsch STA 449 thermoanalyser connected to a quadrupole mass spectrometer (QMS200 Omnistar, Pfeiffer). The measurements were performed with approximately 25mg sample in a temperature range of 30-800°C (10Kpm). For the specific question of determining the remaining water (chemisorbed and physisorbed) in the sample after thermal treatment in various gas atmospheres, the hydrothermally prepared 30%-IrO_x/ATO was heated up in a 21%-O_2/Ar- or 100%-Ar-stream (100 mln min^{-1}, 10 K min^{-1}) using subsequent 1h-steps of 250°C and 350°C.

4.8 TPR

Temperature-programmed reduction (TPR) of the samples was performed in a fixed bed reactor in a 5 vol.% H_2/Ar-stream (80 mln min^{-1}) at a heating rate of 6 K min^{-1}. Due to the high heat release during the low-temperature reduction feature of Ir, the measurements were performed in a temperature range of 30-800°C with approximately 25 mg sample in order to avoid temperature spikes due to massive heat releases. The H_2-consumption was monitored with a thermal conductivity detector (TCD). A molsieve containing tube was installed ahead of the detector as a water trap. The TCD detector was calibrated by reducing a known amount of CuO. The samples were initially kept under Ar-flow for 1h (80 mln min^{-1}) in order to remove physisiorbed water. The comparison of H_2-signals during the initial switch from 100% Ar to 4.92%-H_2/Ar streams before (dark line in Figure S11) and after TPR (red dashed line in Figure S11) allows to quantify the amount of H_2 initially absorbed by the sample. The hydrogen consumption rate profiles were normalized by the moles of compound calculated from the used mass and the molar mass determined as explained in S.I.

4.9 Electron microscopy

For the morphological study of ATO, a Philips CM200FEG microscope operated at 200 kV and equipped with a field emission gun, the Gatan imaging filter, and energy-dispersive X-ray (EDX) analyzer was used for TEM investigations. The coefficient of spherical aberration was Cs = 1.35 mm, and the information limit was better than 0.18 nm. High-resolution images with a pixel size of 0.016 nm were taken at the magnification of 1083000X with a CCD camera. The Ir/ATO-samples were prepared by drop-casting two small drops of sample solution (powder+water) on carbon coated Cu grids. (S)TEM images and EDX elemental mapping were taken on an aberration-corrected JEOL JEM-ARM200 operated at 200 kV. The microscope is equipped with a high angle Silicon Drift EDX detector with the solid angle of up to 0.98 steradians from a detection area of 100 mm^2.

4.10 DRIFTS

Diffuse reflectance infra-red Fourier Transform Spectroscopy (DRIFTS) was recorded with an MCT detector at a resolution of 4 cm^{-1} by accumulating 1024 scans, using a Praying MantisTM high temperature reaction chamber (ZnSe window) placed in a Bruker IFS 66 spectrometer controlled by OPUS software. Measurements were performed in an in-situ cell capable of heat treatment under gas flow conditions (Bronkhorst mass flow controllers). The samples were purged under 10mln min^{-1} flow over night. A background spectrum of pure KBr was performed at the room temperature. The used gases were supplied by Westfalen (99.99% purity at least). Ar was further purified by passing through Hydrosorb and Oxysorb cartridges. The samples were then heated under Ar and 21%-O_2/Ar flows respectively.

4.11 Raman spectroscopy

Raman spectroscopic investigation was performed at 532 nm excitation wavelength using a confocal microscope setup (S&I GmbH, Warstein Germany) equipped with a PyLoN:2kBUV CCD camera and 750 mm focal length of the monochromator (Princeton Instruments). The laser intensity density on the samples was chosen low enough to exclude decomposition of the amporphous IrOx structure. At higher laser intensities, sharp peaks corresponding to the IrO_2-rutile modes appeared, indicating transformation of the amorphous Ir-oxohydroxide into IrO_2 due to local heating. Spectra resemble an average of multiple measurements at different spots of the sample.

4.12 XPS

XPS-analysis of the a.s. 30mol.%-Ir/ATO was performed at room temperature using non-monochromatized Al-Kα-radiation (1486.7 eV) and a hemispherical analyzer (Phoibos 150, SPECS). The binding energy (BE) was calibrated with respect to the Fermi edge.

4.13 Electrochemical measurements

For electrochemical measurements, the samples were deposited on the anode using catalyst inks. Catalyst inks were prepared by suspending 4mg of sample in 6mL Millipore-filtered H_2O, 3.96 mL isopropanol (Sigma Aldrich) and 40 µL of a Nafion® suspension (5%-Nafion® perfluorinated resin solution, Sigma Aldrich). The suspension was sonicated in an ultrasonic bath for 30 min. A rotating ring disk electrode (RDE, Pine Research Instrumentation, 0.2475 cm^2 glassy carbon disk) was used as a working electrode support. Prior to use, the RDE was repeatedly cleaned with Millipore-filtered water and isopropanol, mirror-polished with alumina bead slurries (Buehler, 1 µm and 0.05 µm) on a polishing cloth, rinsed, sonicated for 15 min in isopropanol in an ultrasonic bath and finally rinsed with Millipore water and isopropanol. Defined volumes of catalyst ink were then cast onto the RRDE using a micropipette in order to insure constant iridium-loadings. The loaded anode was dried for 30 min at 60°C. All activity and stability measurements were conducted in a standard electrochemical cell containing approx. 100mL of H_2SO_4 (0.5 mol L^{-1}) distributed between three compartments separated by fine-porosity glass frits. The central and biggest compartment contained the loaded RDE (anode) mounted on a rotator (MSRX, Pine Research Instrumentation) ensuring a constant rotation of 1600 rpm. The reference electrode was a saturated calomel electrode (SCE) at +0.241 V vs. SHE (Standard Hydrogen Electrode), the counter-electrode was a Pt-wire. The electrolyte was constantly purged with nitrogen at least 20 min before measurements started and throughout the data acquisition. Measurements were carried out with a VSP-multichannel potentiostat (Biologic Instruments). All measurements were corrected at 85% for ohmic drop using high-frequency impedance determination of the ohmic

resistance (4 measurements, 100 kHz, 20 mV amplitude, open circuit potential (E_{oc})). Anode potentials E are reported in V vs. Reversible Hydrogen Electrode (RHE). For chronopotentiommetric (CP) experiments, the overpotential needed to obtain a certain current density was used as a measure of the activity and corresponds to a commonly used value in literature.[5, 55] The overpotential has been determined by equation 2 where η is the overpotential and *E* the working electrode potential in V vs. RHE.

$$\eta = E - 1.23 \quad (2)$$

Contributions from MW-ATO, the glassy carbon (GC)-support as well as the dried ink to the OER-currents can be neglected as shown by the corresponding LSV in Figure S5.

Acknowledgements

The authors gratefully acknowledge Jutta Kröhnert (DRIFTS), Jasmin Allan (XRD), Wiebke Frandsen (SEM) and Matthias Friedrich (XPS) for fruitful discussions and support with the various characterization techniques. Financial support came from the German Federal Ministry for Economic Affairs and Energy (BMWi) in the framework of the "Ekolyser"-project (n° 03ESP106D).

Keywords: iridium • oxygen evolution reaction • electrocatalysis • water splitting • chemical energy storage

[1] R. Schlögl, *ChemSusChem* **2010**, *3*, 209-222.
[2] T. R. Cook, D. K. Dogutan, S. Y. Reece, Y. Surendranath, T. S. Teets, D. G. Nocera, *Chem. Rev.* **2010**, *110*, 6474-6502.
[3] D. L. F. Marcelo Carmo, *Int. J. of Hydrogen Energy* **2013**, *38*, 4901-4934.
[4] R. Kötz, S. Stucki, D. Scherson, D. M. Kolb, *J. Electroanal. Chem. Interfacial Electrochem.* **1984**, *172*, 211-219.
[5] C. C. L. McCrory, S. Jung, I. M. Ferrer, S. M. Chatman, J. C. Peters, T. F. Jaramillo, *J. Am. Chem. Soc.* **2015**, *137*, 4347-4357.
[6] T. Reier, M. Oezaslan, P. Strasser, *ACS Catal.* **2012**, *2*, 1765-1772.
[7] Y. Yi, J. Tornow, E. Willinger, M. G. Willinger, C. Ranjan, R. Schlögl, *ChemElectroChem* **2015**, *2*, 1929-1937.
[8] H. Cachet, M. Froment, F. Zenia, *J. Electrochem. Soc.* **1996**, *143*, 442-448.
[9] K. C. Mishra, K. H. Johnson, P. C. Schmidt, *Phys. Rev. B* **1995**, *51*, 13972-13976.
[10] T. Nütz, M. Haase, *J. Phys. Chem. B* **2000**, *104*, 8430-8437.
[11] A. N. Banerjee, S. Kundoo, P. Saha, K. K. Chattopadhyay, *J. Sol-Gel Sci.Technol.* **2003**, *28*, 105-110.
[12] T. Nütz, U. z. Felde, M. Haase, *J. Chem. Phys.* **1999**, *110*, 12142-12150.
[13] A. C. C. Tseung, S. C. Dhara, *Electrochim. Acta* **1975**, *20*, 681-683.
[14] G. Liu, J. Xu, Y. Wang, X. Wang, *J. Mater. Chem. A* **2015**, *3*, 20791-20800.
[15] A. Ganassin, V. Colic, J. Tymoczko, A. S. Bandarenka, W. Schuhmann, *Phys Chem Chem Phys* **2015**, *17*, 8349-8355.
[16] N. Danilovic, R. Subbaraman, K.-C. Chang, S. H. Chang, Y. J. Kang, J. Snyder, A. P. Paulikas, D. Strmcnik, Y.-T. Kim, D. Myers, V. R. Stamenkovic, N. M. Markovic, *J. Phys. Chem. Lett.* **2014**, *5*, 2474-2478.
[17] T. Reier, H. N. Nong, D. Teschner, R. Schlögl, P. Strasser, *Adv. Energy Mater.* **2017**, *7*, 1-8.
[18] S. Cherevko, S. Geiger, O. Kasian, N. Kulyk, J.-P. Grote, A. Savan, B. R. Shrestha, S. Merzlikin, B. Breitbach, A. Ludwig, K. J. J. Mayrhofer, *Catalysis Today* **2016**, *262*, 170-180.
[19] E. Özer, C. Spöri, T. Reier, P. Strasser, *ChemCatChem* **2016**, 8, 1-8.
[20] C. P. De Pauli, S. Trasatti, *J. Electroanal. Chem.* **1995**, *396*, 161-168.
[21] C. P. De Pauli, S. Trasatti, *J. Electroanal. Chem.* **2002**, *538–539*, 145-151.
[22] A. Marshall, B. Børresen, G. Hagen, M. Tsypkin, R. Tunold, *Mater. Chem. Phys.* **2005**, *94*, 226-232.
[23] A. Marshall, B. Børresen, G. Hagen, M. Tsypkin, R. Tunold, *Electrochim. Acta* **2006**, *51*, 3161-3167.
[24] A. T. Marshall, R. G. Haverkamp, *Electrochim. Acta* **2010**, *55*, 1978-1984.
[25] A. T. Marshall, S. Sunde, M. Tsypkin, R. Tunold, *Int. J. Hydrogen Energy* **2007**, *32*, 2320-2324.
[26] S. Ardizzone, C. L. Bianchi, G. Cappelletti, M. Ionita, A. Minguzzi, S. Rondinini, A. Vertova, *J. Electroanal. Chem.* **2006**, *589*, 160-166.
[27] R. Mráz, J. Krýsa, *J. Appl. Electrochem.* **1994**, *24*, 1262-1266.
[28] I. Katsounaros, S. Cherevko, A. R. Zeradjanin, K. J. J. Mayrhofer, *Angew. Chem.* **2014**, *126*, 104; *Angew. Chem. Int. Ed.* **2014**, *53*, 102-121.
[29] M. Carmo, D. L. Fritz, J. Mergel, D. Stolten, *Int. J. Hydrogen Energy* **2013**, *38*, 4901-4934.
[30] T. Reier, Z. Pawolek, S. Cherevko, M. Bruns, T. Jones, D. Teschner, S. Selve, A. Bergmann, H. N. Nong, R. Schlögl, K. J. J. Mayrhofer, P. Strasser, *J. Am. Chem. Soc.* **2015**, *137*, 13031-13040.
[31] T. Reier, D. Teschner, T. Lunkenbein, A. Bergmann, S. Selve, R. Kraehnert, R. Schlögl, P. Strasser, *J. Electrochem. Soc.* **2014**, *161*, F876-F882.
[32] G. Beni, L. M. Schiavone, J. L. Shay, W. C. Dautremont-Smith, B. S. Schneider, *Nature* **1979**, *282*, 281-283.
[33] E. J. Frazer, R. Woods, *J. Electroanal. Chem. Interfacial Electrochem.* **1979**, *102*, 127-130.
[34] M. Vuković, *J. Appl. Electrochem.* **1987**, *17*, 737-745.
[35] M. Bernicke, E. Ortel, T. Reier, A. Bergmann, J. Ferreira de Araujo, P. Strasser, R. Kraehnert, *ChemSusChem* **2015**, *8*, 1908-1915.
[36] S. Cherevko, T. Reier, A. R. Zeradjanin, Z. Pawolek, P. Strasser, K. J. J. Mayrhofer, *Electrochem. Commun.* **2014**, *48*, 81-85.
[37] P. Lettenmeier, L. Wang, U. Golla-Schindler, P. Gazdzicki, N. A. Cañas, M. Handl, R. Hiesgen, S. S. Hosseiny, A. S. Gago, K. A. Friedrich, *Angew. Chem,.* **2016**, *128*, 752-756; *Angew. Chem. Int. Ed.* **2016**, *55*, 742-746.
[38] J. M. Kahk, C. G. Poll, F. E. Oropeza, J. M. Ablett, D. Céolin, J. P. Rueff, S. Agrestini, Y. Utsumi, K. D. Tsuei, Y. F. Liao, F. Borgatti, G. Panaccione, A. Regoutz, R. G.

Egdell, B. J. Morgan, D. O. Scanlon, D. J. Payne, *Phys. Rev. Lett.* **2014**, *112*, 117601.
[39] A. Minguzzi, C. Locatelli, O. Lugaresi, E. Achilli, G. Cappelletti, M. Scavini, M. Coduri, P. Masala, B. Sacchi, A. Vertova, P. Ghigna, S. Rondinini, *ACS Catal.* **2015**, *5*, 5104-5115.
[40] G. K. Wertheim, H. J. Guggenheim, *Phys. Rev. B* **1980**, *22*, 4680-4683.
[41] F. Conrad, C. Massue, S. Kühl, E. Kunkes, F. Girgsdies, I. Kasatkin, B. Zhang, M. Friedrich, Y. Luo, M. Armbrüster, G. R. Patzke, M. Behrens, *Nanoscale* **2012**, *4*, 2018-2028.
[42] V. Pfeifer, T. E. Jones, J. J. Velasco Vélez, C. Massué, R. Arrigo, D. Teschner, F. Girgsdies, M. Scherzer, M. T. Greiner, J. Allan, M. Hashagen, G. Weinberg, S. Piccinin, M. Hävecker, A. Knop-Gericke, R. Schlögl, *Surf. Interface Anal.* **2015**, *48*, 261-273.
[43] V. Pfeifer, T. E. Jones, J. J. Velasco Vélez, C. Massué, M. T. Greiner, R. Arrigo, D. Teschner, F. Girgsdies, M. Scherzer, J. Allan, M. Hashagen, G. Weinberg, S. Piccinin, M. Hävecker, A. Knop-Gericke, R. Schlögl, *Phys. Chem. Chem. Phys.* **2016**, *18*, 2292-2296.
[44] F. Karimi, B. A. Peppley, A. Bazylak, *ECS Transactions* **2015**, *69*, 87-98.
[45] N. Bestaoui, E. Prouzet, P. Deniard, R. Brec, *Thin Solid Films* **1993**, *235*, 35-42.
[46] H.-J. Jeon, M.-K. Jeon, M. Kang, S.-G. Lee, Y.-L. Lee, Y.-K. Hong, B.-H. Choi, *Mater. Lett.* **2005**, *59*, 1801-1810.
[47] J. Zhang, L. Gao, *Mater. Res. Bull.* **2004**, *39*, 2249-2255.
[48] K.-S. Lee, I.-S. Park, Y.-H. Cho, D.-S. Jung, N. Jung, H.-Y. Park, Y.-E. Sung, *J. Catal.* **2008**, *258*, 143-152.
[49] E. N. Balko, P. H. Nguyen, *J. Appl. Electrochem.* **1991**, *21*, 678-682.
[50] K. Kamada, M. Tokutomi, N. Enomoto, J. Hojo, *J. Mater. Chem.* **2005**, *15*.
[51] N. Bestaoui, E. Prouzet, *Chem. Mater.* **1997**, *9*, 1036-1041.
[52] T. Ioroi, N. Kitazawa, K. Yasuda, Y. Yamamoto, H. Takenaka, *J. Electrochem. Soc.* **2000**, *147*, 2018-2022.
[53] D. A. Pankratov, P. N. Komozin, Y. M. Kiselev, *Russ. J. Inorg. Chem.* **2011**, *56*, 1794-1799.
[54] A. M. Cruz, L. Abad, N. M. Carretero, J. Moral-Vico, J. Fraxedas, P. Lozano, G. Subías, V. Padial, M. Carballo, J. E. Collazos-Castro, N. Casañ-Pastor, *J. Phys. Chem. C* **2012**, *116*, 5155-5168.
[55] C. C. L. McCrory, S. Jung, J. C. Peters, T. F. Jaramillo, *J. Am. Chem. Soc.* **2013**, *135*, 16977-16987.
[56] J. M. Spurgeon, J. M. Velazquez, M. T. McDowell, *Phys. Chem. Chem. Phys.* **2014**, *16*, 3623-3631.
[57] R. Sasikala, N. M. Gupta, S. K. Kulshreshtha, *Catal. Lett.* **2001**, *71*, 69-73.
[58] J. F. Moulder, J. Chastain, R. C. King, *Handbook of X-ray photoelectron spectroscopy: a reference book of standard spectra for identification and interpretation of XPS data*, Perkin-Elmer Eden Prairie, MN, **1992**.
[59] H. G. Sanchez Casalongue, M. L. Ng, S. Kaya, D. Friebel, H. Ogasawara, A. Nilsson, *Angew. Chem.* **2014**, *126*, 7297; *Angew. Chem. Int. Ed.* **2014**, *53*, 7169-7172.
[60] S. W. Gaarenstroom, N. Winograd, *J. Chem. Phys.* **1977**, *67*, 3500-3506.
[61] S. Geiger, O. Kasian, B. R. Shrestha, A. M. Mingers, K. J. J. Mayrhofer, S. Cherevko, *J. Electrochem. Soc.* **2016**, *163*, F3132-F3138.
[62] Y. S. Huang, S. S. Lin, C. R. Huang, M. C. Lee, T. E. Dann, F. Z. Chien, *Solid State Commun.* **1989**, *70*, 517-522.
[63] A. Diéguez, A. Romano-Rodríguez, A. Vilà, J. R. Morante, *J. Appl. Phys.* **2001**, *90*, 1550-1557.
[64] M. N. Rumyantseva, A. M. Gaskov, N. Rosman, T. Pagnier, J. R. Morante, *Chem. Mater.* **2005**, *17*, 893-901.
[65] U. Hintermair, S. W. Sheehan, A. R. Parent, D. H. Ess, D. T. Richens, P. H. Vaccaro, G. W. Brudvig, R. H. Crabtree, *J. Am. Chem. Soc.* **2013**, *135*, 10837-10851.
[66] J. Huang, J. D. Blakemore, D. Fazi, O. Kokhan, N. D. Schley, R. H. Crabtree, G. W. Brudvig, D. M. Tiede, *Phys. Chem. Chem. Phys.* **2014**, *16*, 1814-1819.
[67] S. Ito, Y. Abe, M. Kawamura, K. H. Kim, *J. Vac. Sci. Technol., B* **2015**, *33*, 041204.
[68] S. H. Brewer, D. Wicaksana, J.-P. Maria, A. I. Kingon, S. Franzen, *Chem. Phys.* **2005**, *313*, 25-31.
[69] S. Musić, S. Popović, M. Maljković, Z. Skoko, K. Furić, A. Gajović, *Mater. Lett.* **2003**, *57*, 4509-4514.
[70] F. M. Smits, *Bell Syst. Tech. J.* **1958**, *37*, 711-718.

FULL PAPER

MW-produced supported Ir-particles were identified as outstanding electrocatalysts for acidic oxygen evolution reaction (OER). The superior OER-performance could be linked to the nature of the produced $Ir^{III/IV}$-oxohydroxide phase. As a result of the combination of high activitiy and stability, $Ir^{III/IV}$-oxohydroxides are proposed as desirable alternatives to stable but less active IrO_2.

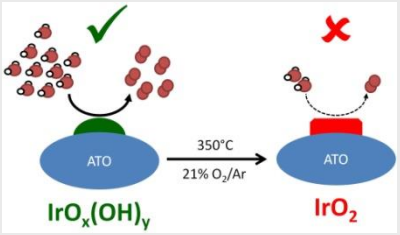

C. Massué, V. Pfeifer, X. Huang, J. Noack, A. Tarasov, S. Cap and R. Schlögl*

Page No. – Page No.
High-performance supported Ir-oxohydroxide water oxidation electrocatalysts